LAWRENCE
LIVERMORE
NATIONAL
LABORATORY

LLNL-JRNL-701357

Linear Calculations of Edge Current Driven Kink Modes with BOUT++ code

G. Q. Li, X. Q. Xu

August 24, 2016

Physics of Plasmas

Disclaimer

This document was prepared as an account of work sponsored by an agency of the United States government. Neither the United States government nor Lawrence Livermore National Security, LLC, nor any of their employees makes any warranty, expressed or implied, or assumes any legal liability or responsibility for the accuracy, completeness, or usefulness of any information, apparatus, product, or process disclosed, or represents that its use would not infringe privately owned rights. Reference herein to any specific commercial product, process, or service by trade name, trademark, manufacturer, or otherwise does not necessarily constitute or imply its endorsement, recommendation, or favoring by the United States government or Lawrence Livermore National Security, LLC. The views and opinions of authors expressed herein do not necessarily state or reflect those of the United States government or Lawrence Livermore National Security, LLC, and shall not be used for advertising or product endorsement purposes.

LLNL-JRNL-701357

Linear Calculations of Edge Current Driven Kink Modes with BOUT++ code*

G.Q. Li[1,2], X.Q. Xu[2], P.B. Snyder[3], A.D. Turnbull[3], T.Y. Xia[1,2], C.H. Ma[2,4], P.W. Xi[2,4]

[1] *Institute of Plasma Physics, CAS, Hefei, Anhui 230031, PRC*
[2] *Lawrence Livermore National Laboratory, Livermore, CA 94550, USA*
[3] *General Atomics, San Diego, CA 92186, USA*
[4] *Peking University, Beijing 100871, PRC*
E-mail: ligq@ipp.ac.cn

Abstract: This work extends previous BOUT++ work to systematically study the impact of edge current density on edge localized modes (ELMs), and to benchmark with the GATO and ELITE codes. Using the CORSICA code, a set of equilibria was generated with different edge current densities by keeping total current and pressure profile fixed. Based on these equilibria, the effects of the edge current density on the MHD instabilities were studied with the 3-field BOUT++ code. For the linear calculations, with increasing edge current density, the dominant modes are changed from intermediate-n and high-n ballooning modes to low-n kink modes, and the linear growth rate becomes smaller. The edge current provides stabilizing effects on ballooning modes due to the increase of local shear at the outer mid-plane with the edge current. For edge kink modes, however, the edge current does not always provide a destabilizing effect; with increasing edge current, the linear growth rate first increases, and then decreases. In benchmark calculations for BOUT++ against the linear results with the GATO and ELITE codes, the vacuum model has important effects on the edge kink mode calculations. By setting a realistic density profile and Spitzer resistivity profile in the vacuum region, the resistivity was found to have a destabilizing effect on both the kink mode and on ballooning mode. With diamagnetic effects included, the intermediate-n and high-n ballooning modes can be totally stabilized for finite edge current density.

1. Introduction

Edge localized modes (ELMs) are an important instability in tokamaks. They are an especially critical issue for ITER and future tokamak reactors, because the high heat flux could damage the divertor and first wall. Nowadays it is widely accepted that the mechanism driving ELMs is the peeling-ballooning (P-B) mode[1–3]. Both the edge current density and pressure gradient play roles in ELM stability, as the edge current gradient driven peeling modes couple with the pressure gradient driven ballooning modes. While GATO[4] provided the first numerical peeling-ballooning mode calculation corresponding to an ELM, the ELITE[2,3] code was developed specifically to be the first successful numerical implementation of the P-B model and is now routinely used to explain the onset of ELMs. After that other linear codes (such as MISHKA[5,6], and MARG2D[7,8]) and nonlinear codes (such as BOUT[9,10], BOUT++[11–13], M3D[14–16], NIMROD[17–19] and JOREK[20]) were developed, and have since been used to explain a number of aspects of ELM behavior.

In BOUT++, the 3-field, two fluid, reduced MHD model was originally implemented[11–13]. In this model, nonideal effects (diamagnetic drift, $E \times B$ drift, resistivity, anomalous viscosity and thermal diffusivity) can be included. Recently, the code was extended to

implement more complicated models such as the 6-field model[21] and gyro-Landau-fluid (GLF) model[22]. This has been successfully used to explain some experiments, and has been benchmarked with other codes[13, 23a-d] . However so far, BOUT++ has been used mainly to study ballooning dominated ELMs. The studies were mainly carried out for a circular cross-section equilibrium sequence with a monotonically decreasing current profile, and without peaks near the edge, designated here as cbm18. This work extends previous BOUT++ work to systematically study the role of edge current in the ELMs, by adding a peak in the current density near the edge with varying magnitude, and benchmarking with the GATO and ELITE codes. GATO and ELITE are community standard codes, based on a linear MHD model, and are often used for code benchmarks; while GATO is an ideal code, appropriate for low-n $(n = 1 - 15)$ modes, ELITE includes some non-ideal effects, particularly sheared rotation, and is valid for intermediate-n $(n = 5 - 100)$ modes.

The equilibrium model for the starting case, cbm18_dens8 is described in section 2. Based on this equilibrium, a sequence of equilibria with different edge current densities was then generated. Section 3, the main section of this paper, studies the role of edge current densities in the ELMs. Also, the linear calculation benchmark with other codes is described. Section 4 provides a summary and some discussion.

2. Equilibrium model

As mentioned in the introduction, so far, the cbm18 equilibrium sequence has mainly been used for the BOUT++ calculations and benchmarks. However, for the cbm18 equilibrium, the flux surface averaged parallel current is small in the edge region (See Figure 1(b) for the parallel current profile) and the instabilities are consequently ballooning dominated. This study extends the previous work to systematically investigate the impact of edge current on the ELMs. Starting from the cbm18_dens8 equilibrium, a sequence of equilibria with different finite edge current densities was then generated to study the effect of edge equilibrium current on the ELMs.

The cbm18_dens8 equilibrium was originally generated with the TOQ code [REFERENCE: MILLER ET AL]. The equilibrium was reproduced with the TEQ equilibrium module in the CORSICA code[23]. TEQ has convenient options for specifying the profiles, and these are utilized to set the edge current density profile. The major parameters of the cbm18_dens8 are: major radius $R_0 = 3.0$ m, minor radius $r = 1.20$ m, vacuum magnetic field at the major radius $B_{T0} = 2$ T, plasma current $I_p = 1.63$ MA, $q_0 = 1.05$, $q_{edge} = 2.99$ and $\beta_N = 1.55$.

Figure 1 shows the plasma geometry and profiles. The equilibrium has a circular geometry, and is extended to include a vacuum region. The presence of a vacuum region permits free-boundary instabilities. For the BOUT++ calculations, the vacuum region is included as a low pressure plasma, and the physical model is the same as in the plasma region. In contrast, for the eigenvalue codes GATO[24] and ELITE[2], the perturbed energy contributed from the vacuum region is calculated with the Greens function method [REFERENCE: TROYON ET AL 1980 AND CHANCE ET AL], so the vacuum region of the equilibrium can be replaced by an extended boundary condition. In figure 1, the red solid line is the plasma boundary, where the pressure and current drop to almost zero. Also the green dashed lines show the computational boundary used for BOUT++, $\psi_{range} = [0.2, 1.4]$. This domain

is larger than was taken in previous calculations ([0.4, 1.2])[11–13], because the kink mode has a wider mode structure. It should be clarified that for the cbm18 equilibrium sequence, the computational boundary (a circle with minor radius $r = 2.0\,m$) is a perfect circle, while the plasma boundary is a little elongated.

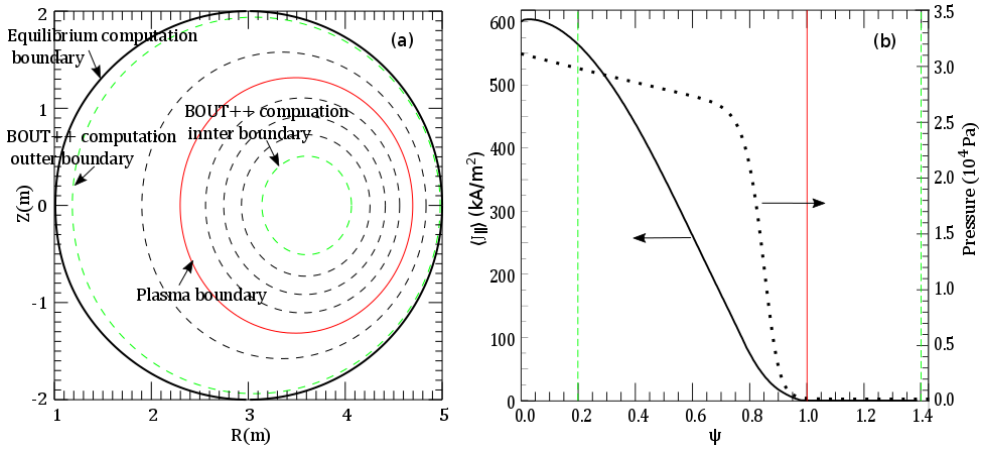

Figure 1. Cbm18_dens8 equilibrium configuration and profiles. (a) Flux surface configuration. (b) Profiles of pressure and flux surface averaged parallel current.

Figure 1(b) shows the pressure profile and flux surface averaged parallel current profile $\langle J_{\parallel}\rangle = \langle \boldsymbol{J}\cdot\boldsymbol{B}\rangle/B_{T0}$. The pressure profile has a large pedestal height, which could lead to a strongly unstable ballooning mode. At the plasma edge, the pressure goes to almost zero; it is actually set to a small value (0.5% of central pressure) to avoid numerical issues. As pointed out earlier and seen in figure 1(b), the cbm18_dens8 equilibrium does not have a peak in the current density near the edge. However, a peak should be present in the current density for an H-mode plasma, due to the bootstrap current from the large edge pressure gradient. Therefore, the sequence of equilibria based on the cbm18_dens8 case, was generated with different edge current densities calculated by scaling the Sauter bootstrap current model[25,26] by different factors. The sequence of edge current density profiles and corresponding safe factor (q) profiles are shown in figure 2. As the edge current density increases, the q profile at the edge changes, so the magnetic shear also changes.

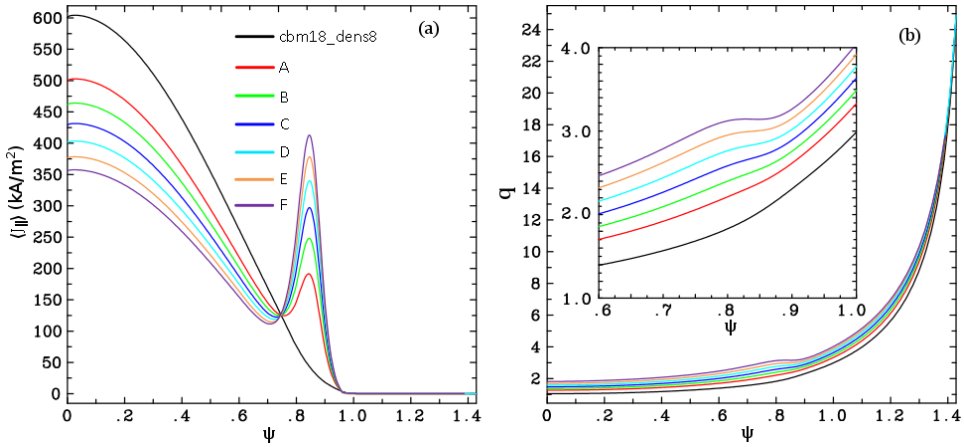

Figure 2. Profiles for the sequence of equilibrium with different edge current density profile. (a) Profiles of flux surface averaged parallel current. (b) Profiles of safety factor. The insert shows the edge region on a finer scale.

As the edge current density profile was changed, the pressure profiles and total current were kept fixed, which is the case in the experiments after the current ramp-up. Furthermore, the plasma current is related to another important stability parameter, $\beta_N = \beta_T/(I/aB_T)$, where $\beta_T = 2\mu_0\langle p\rangle/B_{T0}^2$; the kink mode (both global and edge kink modes) has a strong dependence on β_N, which sets the so-called beta limit[27]. With the total current increasing, β_N will decrease, and this tends to stabilize both the ballooning mode and kink mode. In the present work, the total current was also kept approximately fixed, which generally implies that β_N is almost fixed as well.

3. Impact of edge current density on ELMs

3.1 Physcical model and equations

A 3-field, two-fluid, reduced MHD model is used to study the effect of edge current density. Although the 6-field model is available[21], it was found that the additional physics in the 6-field formulation (ion acoustic waves, thermal conductivities, Hall effects, toroidal compressibility and electron–ion friction) do not qualitatively change the linear instability properties and early phases of ELM dynamics, though those effects are important for self-consistent turbulence and transport and for calculations of the power deposition on the PFCs. The 3-field model is sufficient to simulate the onset of ELMs[21] and is used in this paper. The model and equations were described in Ref.[13]; here we summarily describe them again, but only include the terms that are important for linear calculations. The equations evolve pressure P, vorticity ϖ and perturbed magnetic vector potential $A_\parallel$:

$$\frac{\partial\tilde{\varpi}}{\partial t} + \boldsymbol{v}_E\cdot\nabla\tilde{\varpi} = B_0\nabla_\parallel\tilde{J}_\parallel + 2\boldsymbol{b}_0\times\boldsymbol{k}_0\cdot\nabla\tilde{P} \tag{1}$$

EQUATIONS MISSING THROUGH THIS SECTION $\frac{\partial P}{\partial t} + \boldsymbol{v}_E\cdot\nabla P = 0\,,$ (2)

$$\frac{\partial \tilde{A}_\parallel}{\partial t} = -\nabla_\parallel \Phi + \frac{\eta}{\mu_0}\nabla_\perp^2 \tilde{A}_\parallel, \tag{3}$$

The variables in the equations are defined as:

$$\tilde{\varpi} = \frac{n_0 M_i}{B_0}\left(\nabla_\perp^2 \tilde{\phi} + \frac{1}{n_0 Z_i e}\nabla_\perp^2 \tilde{P}\right), \quad \Phi = \tilde{\phi} + \Phi_0,$$

$$J_\parallel = J_{\parallel 0} - \frac{1}{\mu_0}\nabla_\perp^2 \tilde{A}_\parallel, \ \ \boldsymbol{v}_E = \frac{1}{B_0}(\boldsymbol{b}_0 \times \nabla_\perp \Phi) \tag{4}$$

In the equations, some variables can be written as $F = F_0 + \tilde{F}$, where F_0 represents for the equilibrium part and $\tilde{F}$ is the perturbed component. Here $\nabla_\parallel F = B\partial_\parallel(F/B)$ for any F, $\partial_\parallel = \partial_\parallel^0 + \boldsymbol{b}\cdot\nabla$, $\boldsymbol{b} = \boldsymbol{B}/B = \nabla_\parallel A_\parallel \times \boldsymbol{b}_0/B$, $\partial_\parallel^0 = \boldsymbol{b}_0 \cdot \nabla$, $\boldsymbol{k}_0 = \boldsymbol{b}_0 \cdot \nabla \boldsymbol{b}_0$ is the magnetic field-line curvature vector, η is the resistivity. The important diamagnetic effects are retained in the second term $(1/(n_0 Z_i e)\nabla_\perp^2 \tilde{P})$ of the vorticity expression.

A field-aligned coordinate system is used to solve the equations. The relationship between the field-aligned coordinate system (x, y, z) and conventional toroidal coordinate system (ψ, θ, φ) is:

$$x = \psi - \psi_0, \ \ y = \theta, \ \ z = \varphi - \int_{\theta_0}^{\theta} \nu(\psi, \theta) d\theta. \tag{5}$$

where ν is the local field-line pitch given by

$$\nu(\psi, \theta) = \frac{\boldsymbol{B}\cdot\nabla\varphi}{\boldsymbol{B}\cdot\nabla\theta} \tag{6}$$

and where $h_\theta = 1/|\nabla\theta|$ is the θ scale factor. With field-aligned coordinates, the computational mesh is aligned with the magnetic field, which greatly reduces the number of gird-points needed in this direction. A convergence study showed that for the linear calculation, a grid size of the simulation domain in radial, parallel, and binormal directions $n_x \times n_y \times n_z = 1028 \times 64 \times 16$ points is easily sufficient.

For the linear calculations, in order to benchmark the BOUT++ results with the GATO and ELITE codes, we first focus on the ideal MHD case. Then, the more realistic situation (with the effects of diamagnetic effects, realistic density, and Spitzer resistivity) is considered.

3.2 Linear ideal MHD calculation results

For the linear calculations, different toroidal modes are uncoupled. For each equilibrium and each toroidal mode number (from n = 3 to 45), the calculated growth rate is shown in Figure 3(a) versus toroidal mode number. The cbm18_dens8 case is a ballooning dominated case[19]. The most unstable mode number is at the highest n and the low n kink mode is stable. This case has been studied by BOUT++ and other codes[13,16,19]. Figure 3(a) shows that as the edge current density increases, the dominant mode changes from a high-n ballooning mode to low-n kink mode. For the high n mode, the linear growth rate becomes smaller as the current increases. Thus the edge current density provides a stabilizing effect on the ballooning mode. These trends have been found by other linear codes such as ELITE[28] and MISHKA-1[6].

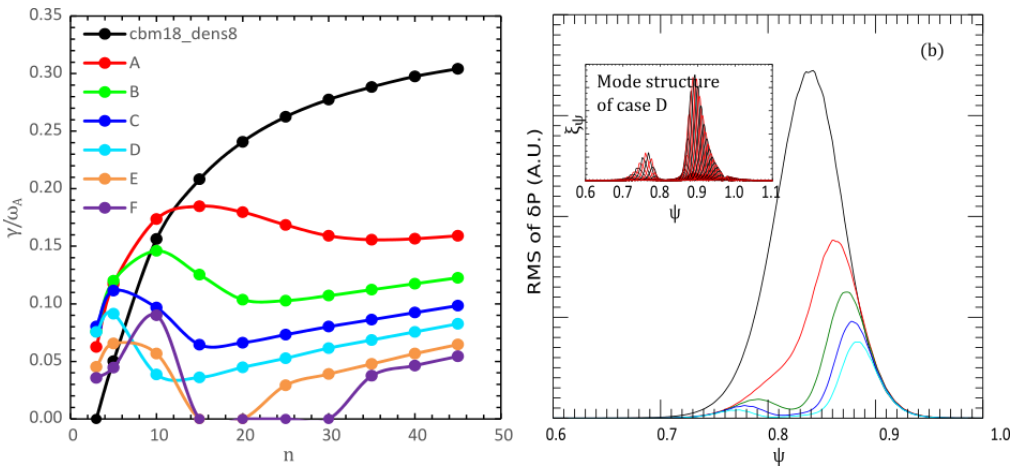

Figure 3. (a) Linear growth rate for cases with different edge current densities. (b) Root mean square of the perturbed pressure profiles for n=35. The Fourier decomposition of $\xi_\psi = \boldsymbol{\xi} \cdot \nabla\psi/|\nabla\psi|$ for the most unstable mode in case D is plotted in the inset..

To clearly see the effect of current stabilization on ballooning modes, the root mean square (RMS) of the perturbed pressure (δP) at the outer mid-plane is plotted in figure 3(b) for the n=35 mode for different edge current densities. The RMS height of δP is normalized to the growth rate in each case. It can be seen that, with the edge current density increasing, the perturbed pressure decreases and a valley forms near ψ ~ 0.825 for the highest edge current density cases. This valley is located at the peak of the current density (figure 2); this stabilization effect is due to the increase in local magnetic shear at the outer mid-plane. Conventionally, the magnetic shear is defined as $s = \frac{r}{q}\frac{dq}{dr}$ or $s = \frac{\psi}{q}\frac{dq}{d\psi}$ or $2V\frac{\partial_\psi q}{\partial_\psi V}$[29] and is an index of the change rate of magnetic field line pitch angle from one flux surface to the next. However, for toroidal geometry, the pitch angle is not uniform in the poloidal direction. Thus, we use the local magnetic shear, defined as

$$s_l = \frac{\psi}{\nu}\frac{d\nu}{d\psi}, \nu = \frac{h_\theta B_\phi}{R B_\theta}, \tag{7}$$

to characterize the local magnetic field properties. Here, the local safety factor, , indicates the local magnetic field pitch angle and h_θ is the radius of curvature. This definition is similar to the global shear, $s = \frac{\psi}{q}\frac{dq}{d\psi}$, but the safety factor q is replaced by the local safety factor ν. The conventional shear definition is essentially the averaged local shear, and here, is referred to as the global shear to avoid confusion. However the ballooning mode is mainly localized at the outer mid-plane where the local shear is the most important. Figure 4 shows the profiles of global shear, local shear at the outer mid-plane and at the inner-plane for the original equilibrium cbm18_den8 and for case D. This shows that, with increasing edge current, the global shear decreases, while the local shear at the outer mid-plane increases in absolute value; it is well known that magnetic shear can stabilize ballooning modes[30].

[THIS DOES NOT SEEM TO BE RIGHT: FROM THE FIGURE IT LOOKS LIKE THE LOCAL OUTER MIDPLANE SHEAR DOES NOT CHANGE FROM CBM18 TO CASE D]

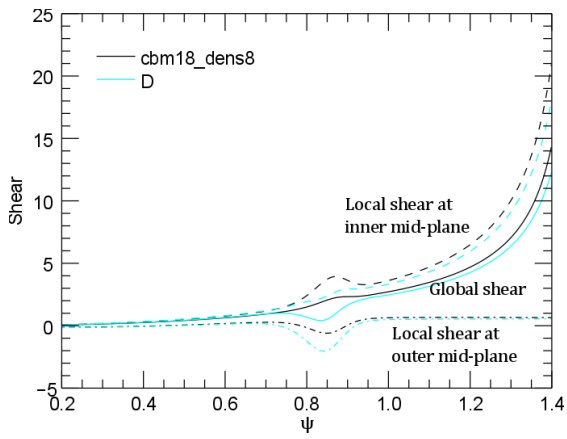

Figure 4. Magnetic global shear ($s = \frac{\psi}{q}\frac{dq}{d\psi}$) and local shear for case cbm18_dens8 and case D.

Figure 3(a) also shows that, as the edge current density increases, the linear growth rate first increases for low-n n kink modes but then decreases. Thus, the edge current density does not always result in a destabilizing effect on the low-n edge kink mode.

3.3 Benchmark with GATO/ELITE codes and the effect of vacuum region

As a check, the BOUT++ results were benchmarked against the GATO and ELITE codes. For the cbm18_dens8 case, the BOUT++ results perfectly agree with GATO/ELITE. Good agreement has also been shown in Ref. 13. However, as the edge current density increases, the difference between BOUT++ and GATO/ELITE becomes apparent. For the low n cases with large edge current density (case D), the difference is especially large.

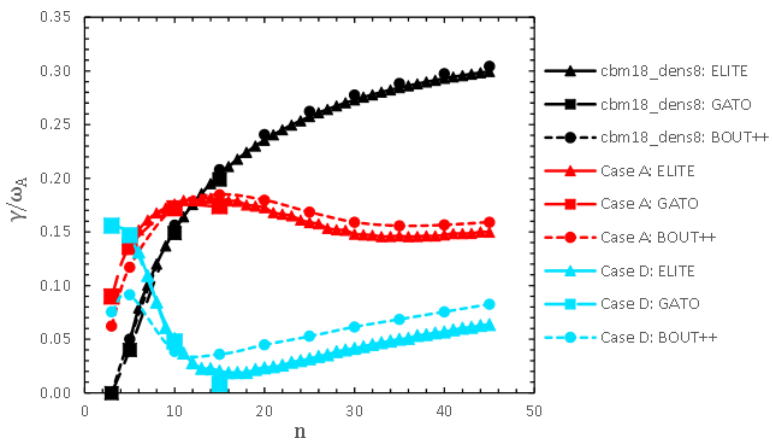

Figure 5. Linear growth rates from BOUT++, ELITE and GATO for cases cbm18_dens8, A, and D.

The discrepancy is due to different physics models in the vacuum region. For GATO and ELITE, the vacuum region is treated as an ideal vacuum, equivalent to a region with an infinite resistivity[19] and the Greens function method is used to calculate the perturbed vacuum energy contribution. On the other hand, for BOUT++, the vacuum region is treated as low pressure plasma. In the previous ideal MHD calculations, this is equivalent to zero resistivity. To demonstrate the effect of vacuum region handling, the plasma boundary used in GATO

was displaced outward by 40% to make the vacuum model the same as in BOUT++. In that case, the linear growth rate and the mode structure from GATO show excellent agreement with the BOUT++ results. Figures 6 (a) and (b) show the growth rate and mode structure from BOUT++ and GATO (for case D, $n = 5$). They are almost identical. For comparison, figure 6(c) also shows the GATO mode structure inside the plasma found with the ideal vacuum model.

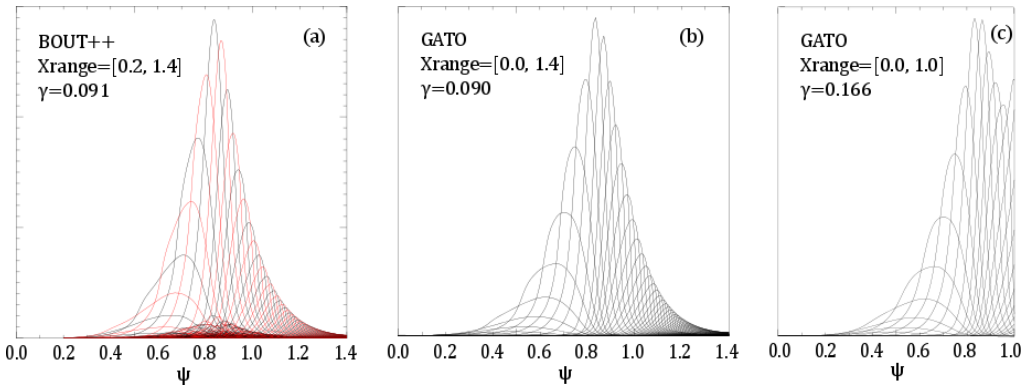

Figure 6. Mode structure comparison for case D, n=5. (a) BOUT++ results. (b) GATO results with computational boundary extended to 1.4. (c) GATO results with normal computational boundary.

The vacuum region handling has an important effect on the low n kink mode calculation. The reason is that the low n kink mode has a wider mode structure than the ballooning mode. As shown in figure 6(a), the mode extends widely into the vacuum region, while for the ballooning dominated case (case cbm18_dens8), the mode structure is relatively narrow, being mostly restricted to the plasma region, and so the vacuum region model has a much smaller effect.

In realistic situations, the vacuum region is neither the ideal vacuum, nor the ideal MHD plasma, but is instead, a highly resistive plasma with low density and low temperature. In the earlier BOUT++ calculations, a constant density and ideal MHD model only were used. The effect of a more realistic density and resistivity therefore needs to be considered. A realistic density profile, defined as $n_e = n_i = C * P^{0.3}$, is shown in figure 7(a). C is selected to obtain a desired $n_e(0)$ value. (Here $n_e(0) = 5 \times 10^{19}\ \mathrm{m}^{-3}$). Then the temperature profile can be calculated from the P profile and assuming $T_e = T_i$. The resistivity is calculated with the Spitzer model:

$$\eta = 0.51 \times 1.03 \times 10^{-4}\, Z_i \ln\Lambda\, T_e^{-3/2}\ \Omega\,\mathrm{m}^{-1} \tag{8}$$

The resistivity profile is also shown in Figure 7(a). The linear growth rates were compared for the cases of constant or realistic density profiles, and ideal or resistive MHD models, and the results for case D are shown in figure 7(b). The realistic density profile has a destabilizing effect on both the ballooning mode and the kink mode. Diamagnetic effects were also considered. It is shown in figure 7(b) that diamagnetic effects are stabilizing for the ballooning mode, but have no effect on the kink mode. With diamagnetic effects, the intermediate n and high n modes can be totally stabilized. As a comparison, the linear growth rate for case cbm18_dens8 is also plotted in figure 7(b). With realistic density, Spitzer

resistivity and diamagnetic effects, the dominant mode is an intermediate n ballooning mode, and the linear growth rate is much higher than in case D. Hence, in the more realistic situation, the edge current can shift the dominant mode from intermediate n ballooning mode to low n kink mode, with a reduction in the linear growth rate.

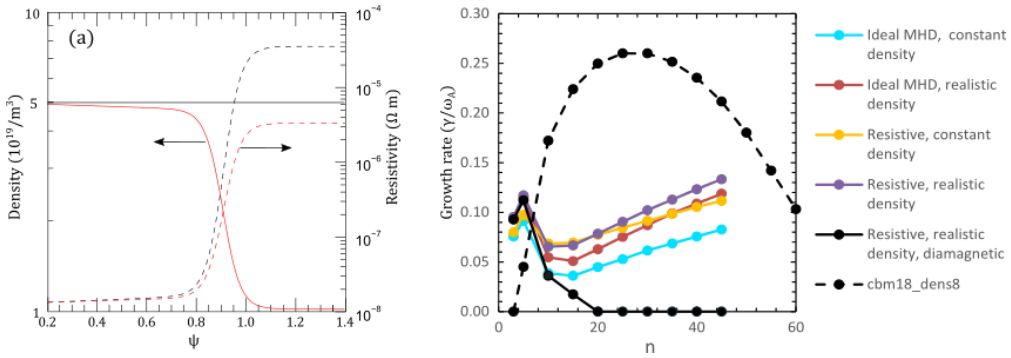

Figure 7. (a) Density and resistivity profiles used in the BOUT++ calculation. The black curves are for constant density and the corresponding resistivity profile, and the red curves are for the realistic density profile. (b) Linear growth rates for Case D with different density and resistivity profiles. With diamagnetic effects included (black solid curve), the intermediate n and high n modes are all stabilized. For case cbm18_dens8 (black dashed curve), the realistic density profile and resistivity and diamagnetic effects are all included.

3.4 High β pedestal plasma cases

One issue of the reduced MHD model used in BOUT++ is that it neglects compressional Alfven waves with $\delta B_{\parallel}\sim 0$, which may become important in high beta plasmas. To determine if the reduced model is still valid for the cases presented here, beta scans were performed and the BOUT++ results compared with GATO results for different β_N^{ped}. The definition of β_N^{ped} is similar to that of β_N in section 2, but with the pressure at the pedestal top substituted for $\langle p\rangle$ in the expression for β_N expression: $\beta_N^{ped} = \beta_T^{ped}/(I/aB_T)$, where $\beta_T^{ped} = 2\mu_0 p^{ped}/B_{T0}^2$. β_N^{ped} is essentially the normalized pedestal height. Figure 8 shows that when the β_N^{ped} reaches 1.8, the difference between the GATO and BOUT++ results becomes apparent. Fortunately in real situations the β_N^{ped} cannot be so large since large Type I ELMs will be triggered before β_N^{ped} reaches 2.0. DIII-D experiments showed that[30] the maximum $\beta_{N,e}^{ped}$ ($\beta_{N,e}^{ped}$ is the electron part of β_N^{ped}) is less than 0.7, so the maximum β_N^{ped} is about 1.4. For ITER, the maximum optimized β_N^{ped} is about 0.9, which was predicted by the EPED1.6 model[31]. We conclude then that for realistic β_N^{ped} values, the reduced MHD model

is still valid for ELM studies.

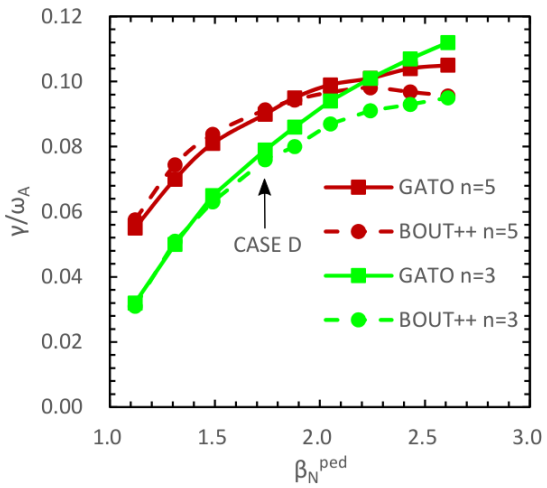

Figure 8. Linear growth rate comparison of GATO and BOUT++ for different β_N^{ped} $(n = 3, 5)$. The difference becomes apparent if $\beta_N^{ped} > 1.8$.

4. Summary

In summary, the impact of edge current density on the ELM behavior has been studied. This work extends previous BOUT++ work to systematically study the impact of edge current density on the ELMs, and provides an additional benchmark with the GATO and ELITE codes. With the 3-field model in the BOUT++ code, the impact of the edge current density on the MHD instabilities was investigated. For the linear calculations, with the edge current density increasing, the dominant modes change from intermediate-n and high-n ballooning modes to low-n kink modes, and the linear growth rate is reduced. The edge current density provides a stabilizing effects on ballooning modes; this stabilizing effect is due to the local shear at the outer mid-plane increasing with the edge current density. For the edge kink modes, the edge current density does not always provide a destabilizing effect; in that case, with the edge current density increasing the linear growth rate first increases, then decreases.

BOUT++ linear results were also benchmarked against the GATO and ELITE codes. It was shown that the vacuum model has an important effect on the edge kink mode calculations. By setting a more realistic density profile and a Spitzer resistivity profile in the vacuum region, the resistivity is found to have a destabilizing effect on both the kink and ballooning modes. With diamagnetic effects included, the intermediate-n and high-n ballooning modes, otherwise destabilized by finite edge current density, can be totally stabilized.

This work shows that with the reduced MHD model, BOUT++ is still valid for kink mode dominated ELM cases, and is still good for high beta cases. A normalized pedestal beta β_T^{ped} is defined to characterize the validity of the reduced MHD model used in BOUT++. However the verification work so far was only performed for a circular plasma. Further verification, validation, and benchmarking with GATO and ELITE for shaped plasmas and diverted plasmas will be given in future publications.

Acknowledgments
This work was supported by the National Magnetic Confinement Fusion Science Program under grant Nos 2014GB106001 and 2013GB111000, and by National Science Foundation of China under grant 10975161. Also performed for USDOE by LLNL under DE-AC52-07NA27344.

References

[1] J. Connor, R. Hastie, H. Wilson, and R. Miller, Phys. Plasmas **5**, 2687 (1998).

[2] P.B. Snyder, H.R. Wilson, J.R. Ferron, L.L. Lao, a. W. Leonard, T.H. Osborne, a. D. Turnbull, D. Mossessian, M. Murakami, and X.Q. Xu, Phys. Plasmas **9**, 2037 (2002).

[3] H.R. Wilson, P.B. Snyder, G.T. a. Huysmans, and R.L. Miller, Phys. Plasmas **9**, 1277 (2002).

[4] T. Osborne, K. Burrell, R. Groebner, L.L. Lao, A.W. Leonard, R. Maingi, R.L. Miller, G.D. Porter, G.M. Staebler, and A.D. Turnbull, J. Nucl. Mater. **266-269**, 131 (1999).

[5] A.B. Mikhailovskii, G.T.A. Huysmans, W.O.K. Kerner, and S.E. Sharapov, Plasma Phys. Reports **23**, 844 (1997).

[6] G. Huysmans, Plasma Phys. Control. Fusion **47**, 165 (2005).

[7] N. Aiba, S. Tokuda, T. Ishizawa, and M. Okamoto, Comput. Phys. Commun. **175**, 269 (2006).

[8] N. AIBA, S. TOKUDA, T. FUJITA, T. OZEKI, M.S. CHU, P.B. SNYDER, and H.R. WILSON, Plasma Fusion Res. **2**, 010 (2007).

[9] X.Q. Xu, R.H. Cohen, T.D. Rognlien, and J.R. Myra, Phys. Plasmas **7**, 1951 (2000).

[10] P.B. Snyder, H.R. Wilson, and X.Q. Xu, Phys. Plasmas **12**, 056115 (2005).

[11] B.D. Dudson, M.V. Umansky, X.Q. Xu, P.B. Snyder, and H.R. Wilson, Comput. Phys. Commun. **180**, 1467 (2009).

[12] X.Q. Xu, B. Dudson, P.B. Snyder, M. V. Umansky, and H. Wilson, Phys. Rev. Lett. **105**, 175005 (2010).

[13] X.Q. Xu, B.D. Dudson, P.B. Snyder, M.V. Umansky, H.R. Wilson, and T. Casper, Nucl. Fusion **51**, 103040 (2011).

[14] W. Park, E. V. Belova, G.Y. Fu, X.Z. Tang, H.R. Strauss, and L.E. Sugiyama, Phys. Plasmas **6**, 1796 (1999).

[15] G. Park, J. Cummings, C.S. Chang, N. Podhorszki, S. Klasky, S. Ku, A. Pankin, R. Samtaney, A. Shoshani, P. Snyder, H. Strauss, L. Sugiyama, and the C. Team, J. Phys. Conf. Ser. **78**, 012087 (2007).

[16] N.M. Ferraro, S.C. Jardin, and P.B. Snyder, Phys. Plasmas **17**, 102508 (2010).

[17] C.R. Sovinec, A.H. Glasser, T.A. Gianakon, D.C. Barnes, R.A. Nebel, S.E. Kruger, D.D. Schnack, S.J. Plimpton, A. Tarditi, and M.S. Chu, J. Comput. Phys. **195**, 355 (2004).

[18] D.P. Brennan, S.E. Kruger, D.D. Schnack, C.R. Sovinec, and A. Pankin, J. Phys. Conf. Ser. **46**, 63 (2006).

[19] B.J. Burke, S.E. Kruger, C.C. Hegna, P. Zhu, P.B. Snyder, C.R. Sovinec, and E.C. Howell, Phys. Plasmas **17**, 032103 (2010).

[20] G.T.. Huysmans and O. Czarny, Nucl. Fusion **47**, 659 (2007).

[21] T.Y. Xia, X.Q. Xu, and P.W. Xi, Nucl. Fusion **53**, 073009 (2013).

[22] X.Q. Xu, P.W. Xi, A. Dimits, I. Joseph, M. V. Umansky, T.Y. Xia, B. Gui, S.S. Kim, G.Y. Park, T. Rhee, H. Jhang, P.H. Diamond, B. Dudson, and P.B. Snyder, Phys. Plasmas **20**, 056113 (2013).

[23a] M. Kim *et al* 2014 **Comparison of measured 2D ELMs with synthetic images from BOUT++ simulation in KSTAR** *Nucl. Fusio* **54** 093004 - M. Kim, M.J. Choi, J. Lee, G.S. Yun, W. Lee, H.K. Park, C.W. Domier, N.C. Luhmann Jr, X.Q. Xu and the KSTAR Team

[23b] H. Y. Guo *et al* 2014 **Recent advances in long-pulse high-confinement plasma operations in Experimental Advanced Superconducting Tokamak** *Phys. Plasmas* **21**, 056107.

[23c] M.E.Fenstermacher, X.Q.Xu, I.Joseph, M.J.Lanctot, C.J.Lasnier, W.H.Meyer, B.Tobias, L.Zeng, A.W.Leonard, T.H.Osborned "**Fast pedestal, SOL and divertor measurements from DIII-D to validate BOUT++ nonlinear ELM simulations**", *Journal of Nuclear Materials*, Volume **438** Supplement, July 2013, Pages S346-S350

[23d] Z. X. Liu, T. Y. Xia, X. Q. Xu, X. Gao, J. W. Hughes, S. C. Liu, S. Y. Ding, and J. G. Li, **ELMy H-mode linear simulation with 3-field model on experimental advanced superconducting tokamak using BOUT++**, *Phys. Plasmas* **19**, 102502 (2012).

[23] J.A. Crotinger, L. LoDestro, L.D. Pearlstein, A. Tarditi, T.A. Casper, and E.B. Hooper, *LLNL Report UCRL ID-126284*, *NTIS #PB2005-102154* (1997).

[24] L. Bernard, F. Helton, and R. Moore, Comput. Phys. Commun. **24**, 377 (1981).

[25] O. Sauter, C. Angioni, and Y. Lin-Liu, Phys. Plasmas **6**, 2834 (1999).

[26] O. Sauter, C. Angioni, and Y.R. Lin-Liu, Phys. Plasmas **9**, 5140 (2002).

[27] A.D. Turnbull, D.P. Brennan, M.S. Chu, L.L. Lao, J.R. Ferron, A.M. Garofalo, P.B. Snyder, J. Bialek, I.N. Bogatu, J.D. Callen, M.S. Chance, K. Comer, D.H. Edgell, S. a. Galkin, D. a. Humphreys, J.S. Kim, R.J. La Haye, T.C. Luce, G. a. Navratil, M. Okabayashi, T.H. Osborne, B.W. Rice, E.J. Strait, T.S. Taylor, and H.R. Wilson, Nucl. Fusion **42**, 917 (2002).

[28] P.B. Snyder, N. Aiba, M. Beurskens, R.J. Groebner, L.D. Horton, a. E. Hubbard, J.W. Hughes, G.T. a. Huysmans, Y. Kamada, a. Kirk, C. Konz, a. W. Leonard, J. Lönnroth, C.F. Maggi, R. Maingi, T.H. Osborne, N. Oyama, a. Pankin, S. Saarelma, G. Saibene, J.L. Terry, H. Urano, and H.R. Wilson, Nucl. Fusion **49**, 085035 (2009).

[29] R.L. Miller, M.S. Chu, the I.D.W. Group, Y.R. Lin-Liu, and R.E. Waltz, Phys. Plasmas **5**, 973 (1998).

[30] J. Greene and M. Chance, Nucl. Fusion **453**, (1981).

[31] P.B. Snyder, R.J. Groebner, J.W. Hughes, T.H. Osborne, M. Beurskens, a. W. Leonard, H.R. Wilson, and X.Q. Xu, Nucl. Fusion **51**, 103016 (2011).

ADDITIONAL REFERENCES:

R. L. Miller, Y. R. Lin-Liu, A. D. Turnbull, V. S. Chan, L. D. Pearlstein, O. Sauter, and L. Villard, Phys. Plasmas **4**, 1062 ~1997

F. Troyon, L. C. Bernard, and R. Gruber, *Computer Physics Communications* 19, 161 (1980).

M.S. Chance, A.D. Turnbull, P.B. Snyder, Journal of Computational Physics (2006)